Article

In Situ Tracking of Colloidally Stable and Ordered Assemblies of Gold Nanorods

Dorota Grzelak, Piotr Szustakiewicz, Christopher Tollan, Sanoj Raj, Petr Král,* Wiktor Lewandowski,* and Luis M. Liz-Marzán*

Read Online

ACCESS | Metrics & More | Article Recommendations | Supporting Information

ABSTRACT: Solution-phase self-assembly of anisotropic nanoparticles into complex 2D and 3D assemblies is one of the most promising strategies toward obtaining nanoparticle-based materials and devices with unique optical properties at the macroscale. However, controlling this process with single-particle precision is highly demanding, mostly due to insufficient understanding of the self-assembly process at the nanoscale. We report the use of in situ environmental scanning transmission electron microscopy (Wet-STEM), combined with UV/vis spectroscopy, small-angle X-ray diffraction (SAXRD) and multiscale modeling, to draw a detailed picture of the dynamics of vertically aligned assemblies of gold nanorods. Detailed understanding of the self-assembly/disassembly mechanisms is obtained from real-time observations, which provide direct evidence of the colloidal stability of side-to-side nanorod clusters. Structural details and the forces governing the disassembly process are revealed with single particle resolution as well as in bulk samples, by combined experimental and theoretical modeling. In particular, this study provides unique information on the evolution of the orientational order of nanorods within side-to-side 2D assemblies and shows that both electrostatic (at the nanoscale) and thermal (in bulk) stimuli can be used to drive the process. These results not only give insight into the interactions between nanorods and the stability of their assemblies, thereby assisting the design of ordered, anisotropic nanomaterials but also broaden the available toolbox for in situ tracking of nanoparticle behavior at the single-particle level.
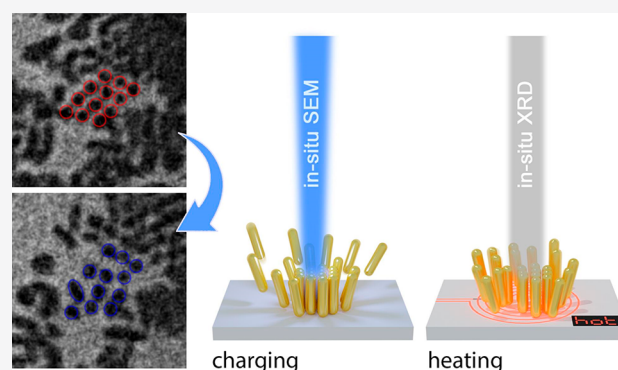
INTRODUCTION

Ordered assemblies of gold nanorods (AuNRs) offer extraordinary properties with potential applications in various technologies, such as chemical and biological sensing,[1−3] in vivo medical studies,[4,5] catalysis,[6−8] data storage,[9] and optoelectronics.[10] The main reason for such a broad applicability is that these materials translate the anisotropic functionality of single particles into micro/macro-(ensemble) scale anisotropy. However, building ordered structures out of AuNRs still poses a significant challenge, due to our limited knowledge regarding the dynamics of the self-assembly process. This limitation largely results from our current inability, either to monitor in situ the behavior of thousands of nanoparticles at the macro-scale (e.g., via UV/vis spectroscopy)[11] or to take ex situ snapshots at the single particle level from static structures (e.g. via electron microscopy).[12] Development of methods for in situ monitoring the behavior of single AuNRs in solution should bring us closer to a complete understanding of the self-assembly mechanism and achieving full control over this process.

In situ electron microscopy (EM) observation of nanoparticle dispersions under dynamic conditions has recently allowed for real-time visualization of chemical and physical events at the single nanoparticle level. Some remarkable examples include the observation of how spherical[13] and anisotropic nanoparticles grow,[14] nanoparticle surface oxidation,[15] or dehydrogenation.[16] More recently, in situ EM has also been used to investigate self-assembly processes. It allowed, e.g., to analyze the influence and contribution of hydrophobic,[17] van der Waals,[18] and electrostatic forces[19] on the kinetics and the outcome of the self-assembly process. However, most of the reported in situ investigations are concerned with the assembly of spherical nanoparticles, and the acquired knowledge cannot be directly translated to the self-assembly principles of anisotropic nanoparticles, since the latter exhibit anisotropic interactions and yield complex 3D
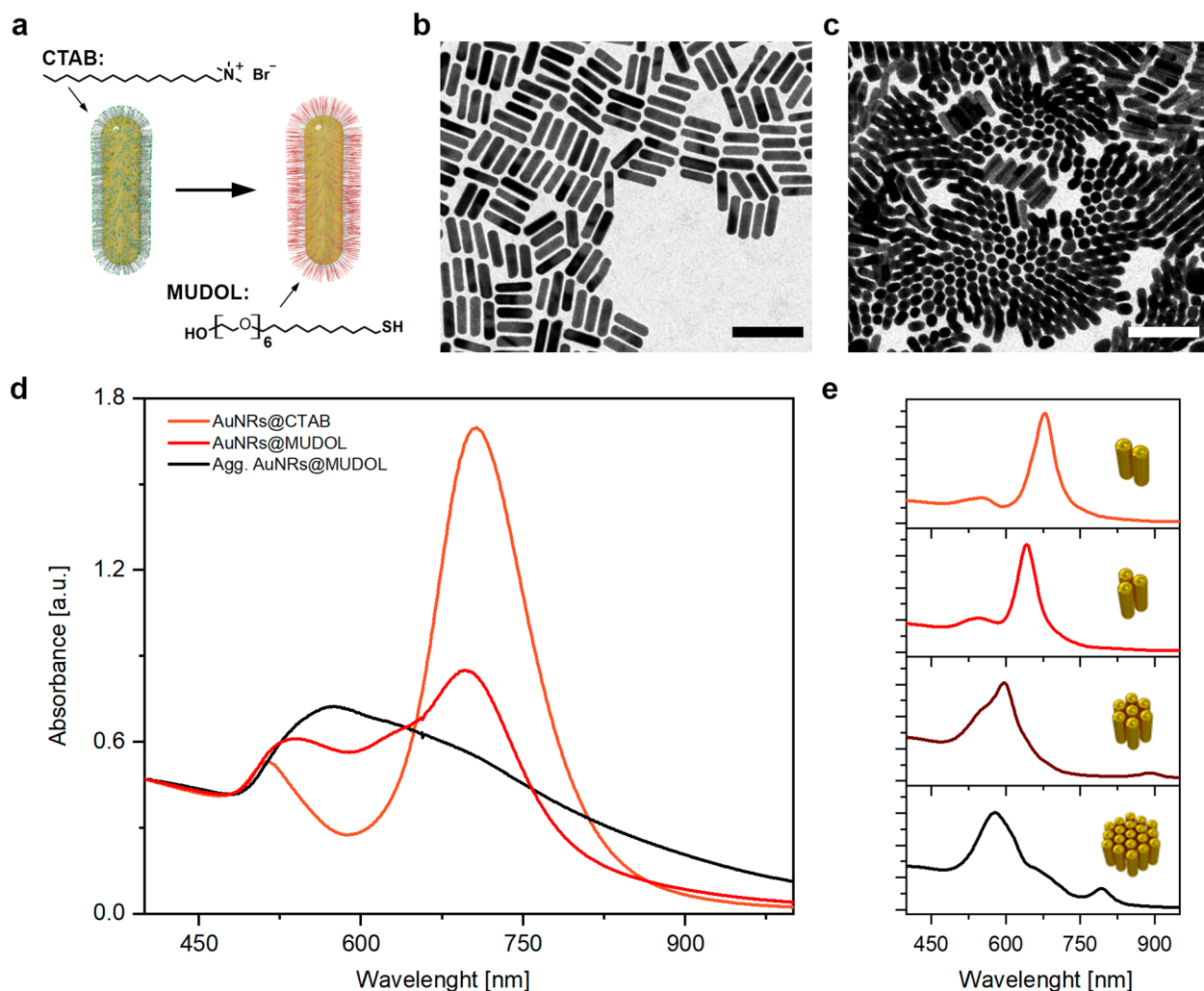
Figure 1. Synthesis and characterization of AuNRs. (a) Scheme of the ligand exchange reaction performed on AuNR@CTAB, to obtain AuNR@MUDOL. (b) Representative TEM image of horizontally deposited AuNR@CTAB assemblies. (c) Representative TEM image of vertical AuNR@MUDOL assemblies. (d) UV/vis spectra of AuNR@CTAB (orange), AuNR@MUDOL directly after ligand exchange (red) and 2 h after completing the ligand exchange reaction (black); spectra were normalized at 400 nm. (e) FDTD-modeled UV/vis spectra for AuNR assemblies comprising two, three, seven, and 19 parallel nanorods.

architectures with orientational order, as well as potential polymorphic behavior.[20−22]

Recent reports have focused on in situ imaging of the self-assembly of anisotropic nanoparticles, providing insight into the behavior of nanocubes,[17] branched nanooctapods,[23] and nanoprisms.[24,25] In the case of NRs two reports on in situ imaging should be highlighted. Alivisatos et al.[26] analyzed trajectories of hexadecyltrimethylammonium bromide (CTAB)-coated AuNRs, revealing long-range and highly anisotropic electrostatic repulsion forces that lead to tip-selective nanorod attachment. Mirsaidov et al.[27] followed the assembly of cysteamine-coated AuNRs at different concentrations of linker molecules, leading to the selective formation of either tip-to-tip or side-to-side clusters. These reports confirm that studying anisotropic nanoparticle interactions at the single particle level provides useful information on their self-assembly. However, these reports focus only on the formation of 1D, few-nanoparticle clusters. Of more general interest but also significantly more challenging is the in situ characterization of assembly and disassembly processes within larger, long-range-ordered assemblies of higher dimensionality. An interesting example in this direction has been recently

reported for the case of triangular Au nanoprisms, which revealed new information on the crystallization of such nanoparticles, further confirming the importance of single-particle level observations of the self-assembly of anisotropic nanoparticles.[25] This is especially important regarding vertical assemblies of nanorods.[10,12] Although early in situ EM studies enabled the observation of large, vertical assemblies of AuNRs, the time scale of the experiments did not allow the observation of single particle events or any qualitative and/or quantitative analysis of the behavior in solution.[28]

In this work, we demonstrate the use of environmental scanning transmission electron microscopy (WetSTEM[28]) to characterize in situ the dynamics of relatively large, 2D, vertical assemblies of AuNRs in the wet state. We were able to monitor the dynamics of single nanoparticles and track the self-assembly and disassembly pathways, for orientationally ordered AuNR aggregates. By combining results of in situ EM, atomistic modeling and ensemble measurements (small-angle X-ray diffraction and UV/vis spectroscopy), we can describe the colloidal stability of side-to-side organized nanorod clusters in solution, thereby gathering insights into the self-assembly mechanism. Additionally, we observe that AuNRs can preserve
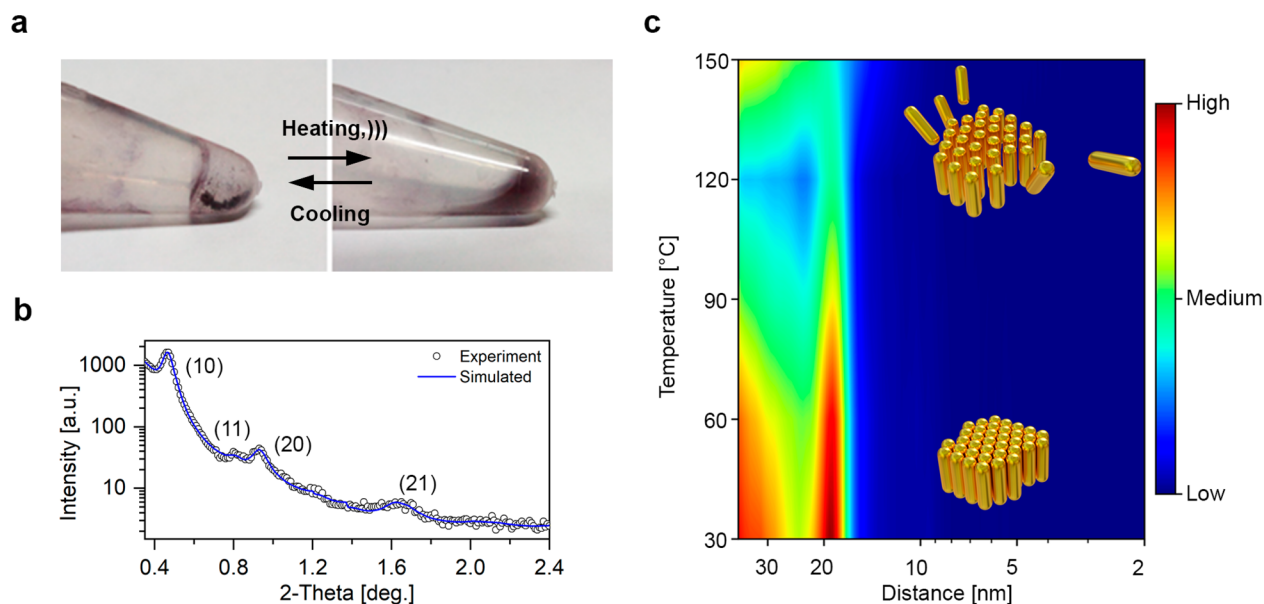
Figure 2. Dynamic self-assembly of AuNR@MUDOL. (a) Photographs of an Eppendorf tube containing precipitated AuNR@MUDOL, 2 h after ligand exchange and the same vial after heating and sonication, evidencing redispersion of AuNR aggregates. (b) 1D SAXRD diffractogram of AuNR@MUDOL, collected at 30 °C. (c) Temperature evolution of SAXRD diffractograms for AuNR@MUDOL aggregates in a 30−150 °C temperature range; two distinct areas can be distinguished: low temperature phase (2D, hexagonal, 30−120 °C) and isotropic phase (120−150 °C).

their orientational order during disassembly and confirm through both experiments and theoretical modeling that both electrostatic and thermal stimuli can play a major role in the process.

RESULTS AND DISCUSSION

Synthesis and Static Characterization of AuNR@MUDOL Assemblies. Gold nanorods are arguably the most widely used nonspherical nanoparticles, due to the relative simplicity of their synthesis and to their outstanding plasmonic properties. The AuNRs used in this work were synthesized by following a seed-mediated method,[29] and synthetic details are given in the Experimental Section. As-obtained AuNRs, 52 × 16 nm (Supporting Information, Figure S1), were stabilized by CTAB (AuNR@CTAB).[30] Although some reports have demonstrated the formation of 3D oriented arrays of AuNR@CTAB,[31] the formation and stability of extended supercrystals is known to be enhanced upon exchanging CTAB molecules with (1-mercaptoundec-11-yl)hexa(ethylene glycol) (MUDOL) ligands (Figure 1a).[32,33] AuNR@MUDOL have lower surface charge and display lower colloidal stability in aqueous dispersions as compared to AuNR@CTAB, and as a consequence, stronger side-to-side interactions have been proposed to lead to parallel aggregation and subsequent deposition as vertical assemblies (induced by the Marangoni effect).[10] Under the same experimental conditions, we confirmed that TEM images of drop-casted AuNR@CTAB resulted in horizontally oriented AuNR assemblies (Figure 1b), whereas for AuNR@MUDOL, multiple vertically oriented AuNR domains were evidenced (Figure 1c). The measured center-to-center distances between nanorods within the observed vertical domains were ∼20 nm, which is reasonable given the diameter of AuNRs (∼16 nm) and the thickness of the organic coating (∼2 nm).[12] To further confirm successful ligand exchange, and to get insight into the colloidal behavior of Au nanorods, we carried out UV/vis spectroscopy

measurements. AuNR@CTAB exhibit two localized surface plasmon resonance (LSPR) bands, corresponding to transverse and longitudinal modes, with maxima at 511 and 707 nm, respectively, which are characteristic of noninteracting, well-dispersed particles. After ligand exchange, the AuNR@MUDOL dispersion exhibits two maxima at 536 and 695 nm, suggesting the formation of colloidal AuNR clusters.[34] When the same dispersion was measured 2 h after completing ligand exchange, we observed a further blue shift and damping of the longitudinal LSPR band, along with a redshift of the transverse band, resulting in a single, broad band with a maximum at 562 nm (Figure 1d). To understand the origin of the observed changes in the plasmonic properties of AuNR@MUDOL, in terms of their assembly state, we performed electromagnetic modeling of side-to-side ordered AuNR clusters. Extinction spectra for AuNRs (with dimensions corresponding to those used in the experiments) were modeled using the finite difference time domain (FDTD) method (see the Experimental Section for details).[35] We focused on five different scenarios: a single AuNR and aggregates comprising two, three, seven, and 19 AuNRs. As shown in Figure 1e, the modeled spectra reveal a gradual blue-shift and broadening of the LSPR band for a growing number of particles in the cluster. This is in agreement with our experimental results (Figure 1d) and with previous examples in the literature,[36] so we can conclude that the observed changes in absorbance spectra for AuNR@MUDOL result from the gradual aggregation of nanorods into parallel clusters, in the aqueous phase. The above-discussed results from bulk characterization of AuNR@MUDOL dispersions confirm their tendency to form side-to-side assemblies in solution, which would result in the formation of vertically aligned assemblies on a substrate. Although the latter is known from the literature,[10,12] the reversibility of such an aggregation process has not been reported.
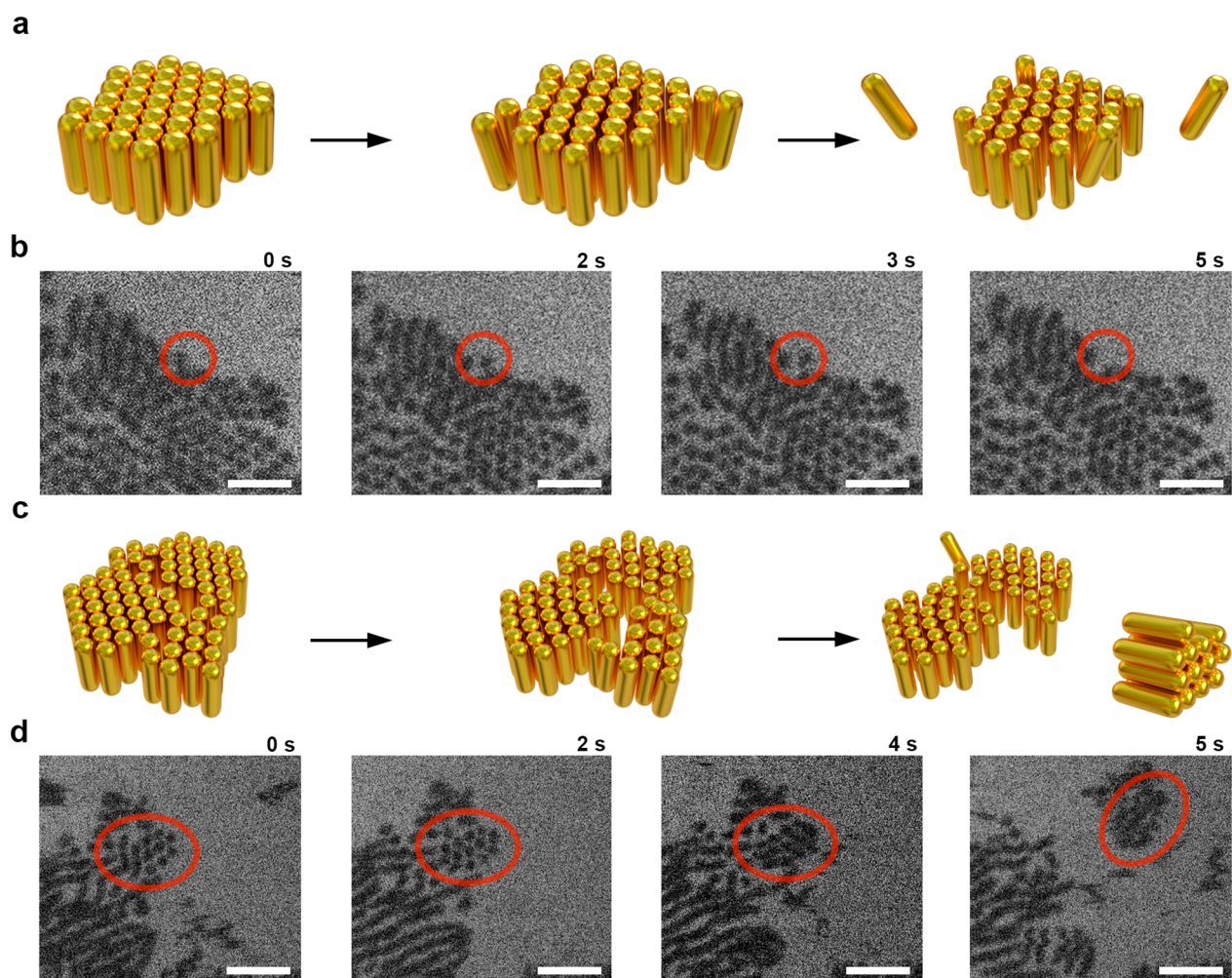
Figure 3. WetSTEM characterization of AuNR@MUDOL. (a) Schematic model of vertically aligned AuNR@MUDOL and single nanoparticle displacement events. (b) WetSTEM images of an AuNR@MUDOL vertical aggregate, showing a single nanoparticle detaching from the aggregate. In the first three frames, we highlight an area containing three AuNRs; after 5 s one AuNR is seen to leave the aggregate (Movie S1). (c) Schematic representation of the observed AuNR@MUDOL behavior, displacement and movements of vertically ordered AuNR clusters. (d) WetSTEM images of an AuNR@MUDOL vertical aggregate, showing an example of AuNR cluster displacement; the apparent changes in cluster appearance are due to variations in the orientation of nanorods with respect to the observation direction; this effect evidences dynamic movements of small side-to-side, 2D ordered clusters (Movie S2).

Bulk Investigation of the Dynamic Self-Assembly of AuNR@MUDOL. Compounds comprising polymeric and oligomeric ethylene glycol moieties are known to exhibit thermoresponsive behavior.[37−39] In the case of self-assembled monolayers, a temperature increase can lead to change of intra- and intermolecular interactions and enable more efficient interactions with water molecules.[40] Thus, when the formation of a precipitate was observed by eye (Figure 2a) in an aged sample of AuNR@MUDOL, we proceeded to heat it and watch whether the nanoparticles get thereby redispersed. Indeed, after heating for 10 min, we observed that the color of the dispersion turned purple, similar to that observed right after ligand exchange, thus confirming the reversibility of self-assembly. The time required to observe AuNR disassembly was of only tens of seconds if sonication was used additionally to heating. Importantly, our experiments confirm that the assembly process can be reversed, however, after 3 consecutive cycles of UV/vis measurements revealed a 4 nm redshift and 20% decrease of intensity of the longitudal LSPR band (Supplementary Note 1).

To study in detail the reversibility of the self-assembly of AuNR@MUDOL, we used small angle XRD (SAXRD). AuNR@MUDOL were initially dispersed in water, which intrinsically limited the temperature range for the measurements. Therefore, we transferred AuNR@MUDOL into glycerol, which has similar dielectric properties to water but a higher boiling point. AuNR@MUDOL in glycerol was allowed to precipitate and then carefully transferred to a glass capillary for temperature-dependent SAXRD measurements. We first collected 1D diffractograms at 30 °C (Figure 2b), which revealed the presence of several Bragg peaks, indicating the formation of long-range ordered assemblies. This pattern was fitted using a 2D hexagonal unit cell, with a dimension (nearest neighbor distance between nanoparticles) of ∼22 nm. This is slightly longer than the value derived from TEM (∼20 nm), in agreement with the dry state of the samples in TEM, while glycerol as a solvent may infiltrate in between the nanoparticles.[41] Hexagonal packing of AuNRs within vertical assemblies has been previously reported, for both monolayers and complex, 3D smectic assemblies.[12] In our SAXRD measurements, we did not observe peaks corresponding to
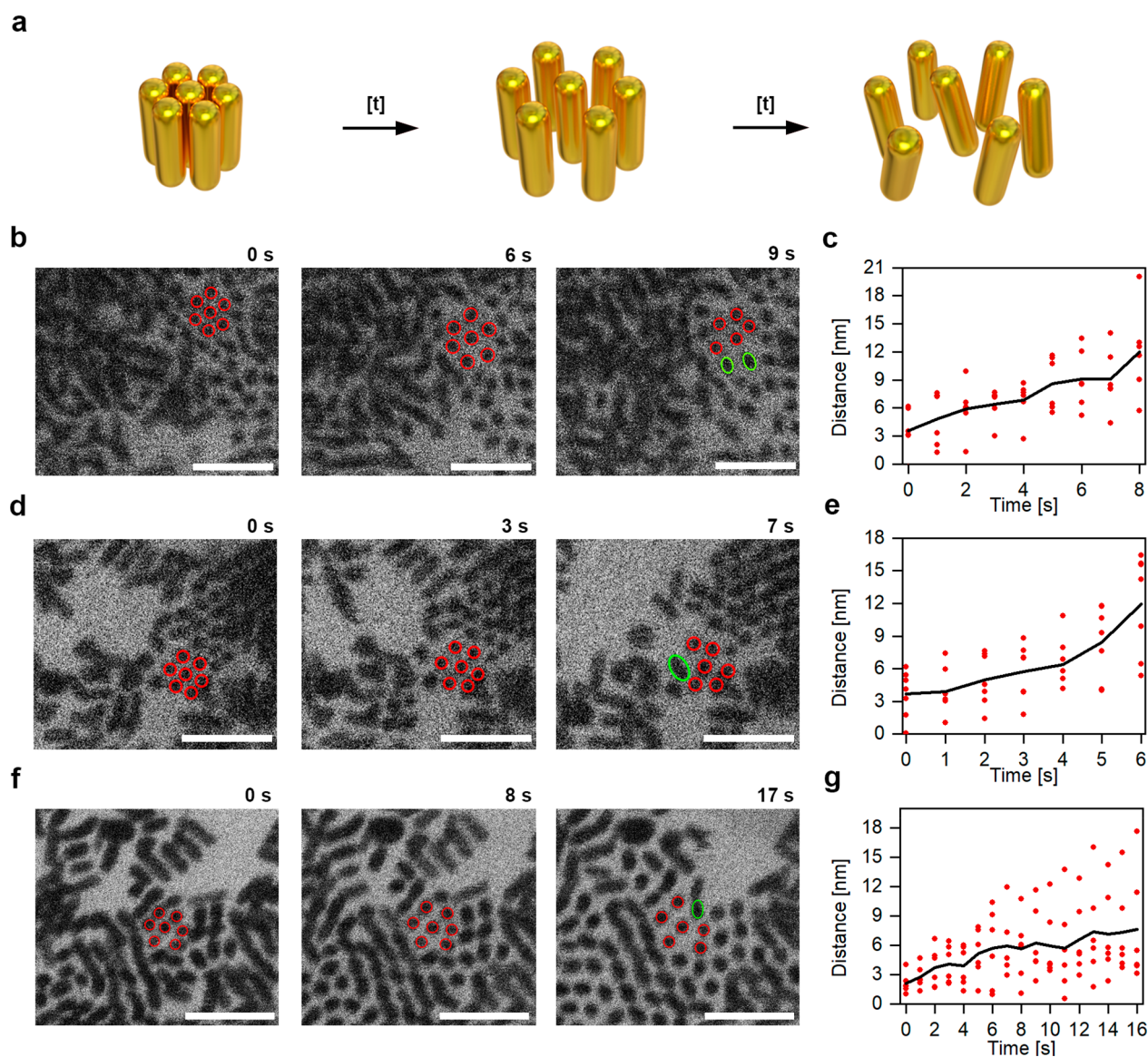
Figure 4. WetSTEM characterization of orientational order within AuNR@MUDOL aggregates. (a) Schematic model of the observed phenomena. (b,d,f) Time-lapse images from in situ WetSTEM recordings of the disassembly of an AuNR@MUDOL aggregate; AuNR clusters for which calculations of interparticle distances were performed are highlighted with red circles; green circles highlight tilted AuNRs, which lost their initial orientational correlation with respect to the rest of the cluster (Movies S6–S8). (c,e,g) Evolution of interparticle distance (surface-to-surface) within the clusters imaged in (b,d,f). Red dots represent distances between pairs of AuNRs, while the solid black line is the averaged value.

multilayer stacking of nanorods, but it should be noted that this signal would appear at angles beyond the sensitivity of our in-house SAXRD instrument.

We then performed temperature-dependent SAXRD measurements. The sample was heated from 30 °C up to 200 °C and diffractograms were collected every 10 °C (Figure 2c). To prevent heat-induced nanoparticle degradation, the acquisition time was kept relatively short (60 s), and therefore we focused on following the evolution of the main (10) Bragg peak, which was visible up to ~135 °C. When approaching this temperature, the peak intensity lowered, indicating a slow disintegration of the aggregates (lower nanoparticle correlation length). Above 135 °C no sharp Bragg peaks were observed but only a broad scattering around the primary beam, which evidenced an isotropic distribution of nanoparticles in the solvent, without orientational order. These results confirm our initial bulk-scale observations.

Nanoscopic Investigation of the Dynamic Self-Assembly of AuNR@MUDOL. To study the self-assembly of AuNR@MUDOL in more detail, we employed in situ electron microscopy imaging of the particles in a liquid. In contrast to TEM-based methods for the examination in liquid, WetSTEM does not require the use of microfluidic devices. We simply drop-casted a dispersion of AuNR@MUDOL in water/ glycerol (1:1 v/v) on top of a standard carbon-coated TEM grid and placed it inside a precooled STEM device. The use of a water/glycerol suspension ensured similar conditions to those previously used in bulk SAXRD measurements. However, a much lower temperature of 2 °C and a reduced pressure of 700 Pa were used in WetSTEM experiments, which made the comparison with bulk measurements less accurate. As a first observation, we confirmed the tendency of AuNR@ MUDOL to self-assemble into vertically oriented arrays (Figure 3), in agreement with TEM imaging of samples
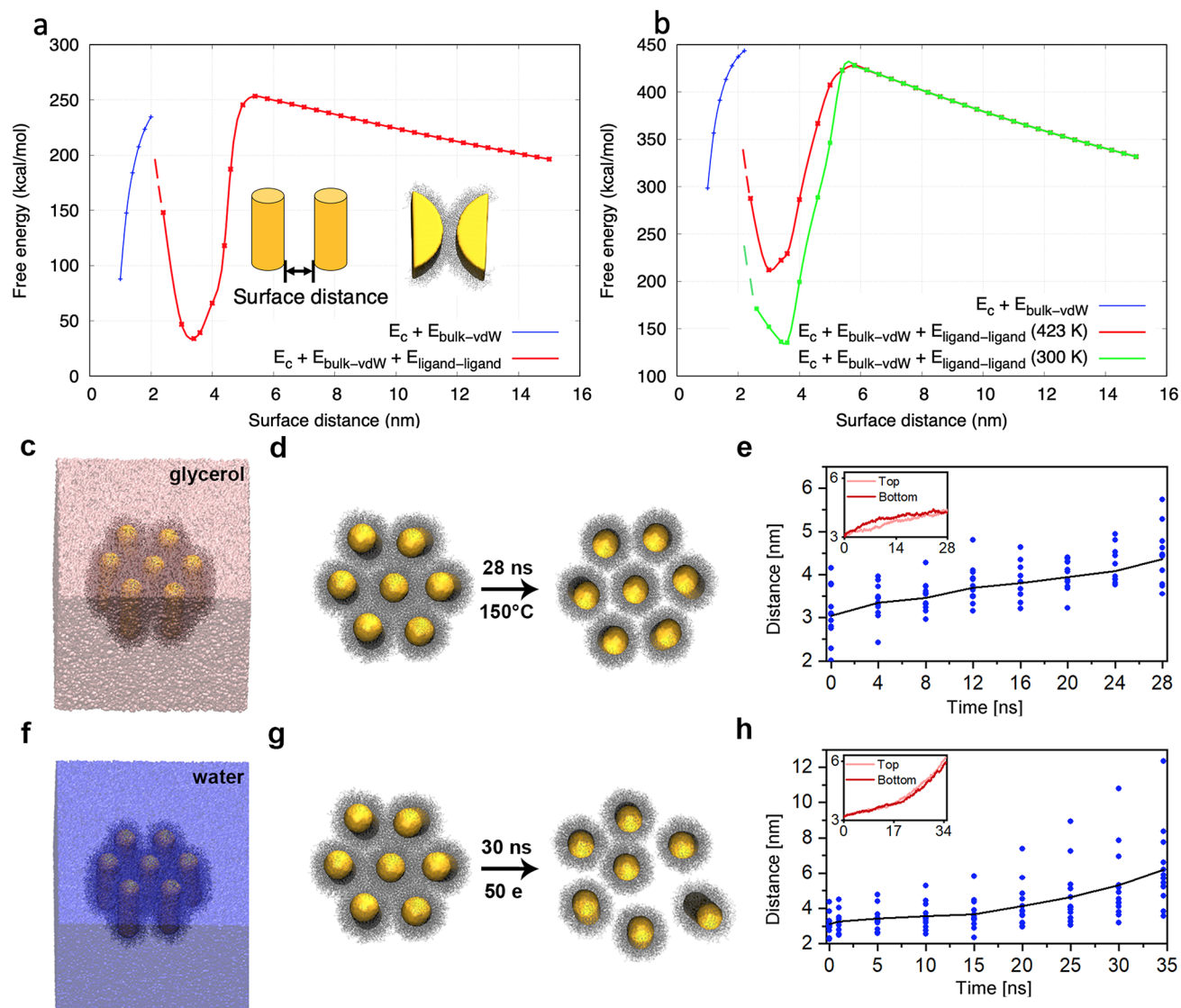
Figure 5. Mean-field modeling of the interactions between AuNRs and MD simulations of stimuli-driven disassembly of small AuNR@MUDOL clusters. (a) Total interaction free energy ($E_{vdW} + E_C + E_{ligand-ligand}$, red dots) at 300 K between AuNRs (52×16 nm) with water as solvent and 130 e charge on the NRs. Solid lines are given for eye guidance. In the right inset two 5 nm-thick slices from 52×16 nm AuNRs at a surface distance of 3.6 nm are shown, which were considered in the MD simulation to estimate the ligand−ligand coupling. Solvent molecules are removed for clarity. (b) Total interaction free energy ($E_{vdW} + E_C + E_{ligand-ligand}$) at two different temperatures (27 and 150 °C), between AuNRs (52×16 nm) in glycerol, assuming 130 e charge on the NRs. Solid lines are given for eye guidance. (c) Corner-view of small AuNRs fully submerged in glycerol at 25 °C. (d) Disassembly of small neutral AuNRs at high temperature (150 °C) in glycerol (snapshots from Movie S9). (e) Time evolution of distances between AuNRs (surface-to-surface) within an AuNR cluster at high temperature (150 °C) in glycerol (data corresponding to the simulation shown in panel d). Blue dots represent distances between pairs of AuNRs, while the solid black line is the averaged value. (inset) The same time-dependent averaged distances are shown separately for the top and bottom ends of AuNRs. (f) Corner-view of the small AuNRs on the surface of water at 25 °C. (g) Disassembly of small charged (50 e) AuNRs in bulk water at 25 °C (snapshots form Movie S10). (h) Time evolution of the distances between charged AuNRs (surface-to-surface) within an AuNR cluster in bulk water at 25 °C. (inset) The same time-dependent averaged distances are shown separately for the top and bottom ends of AuNRs (data corresponding to the simulation shown in panel g).

prepared at ambient pressure. Second, we consistently observed fluctuations of the nanoparticles within the solvent—trembling, twisting, assembling, and disassembling—often similar to previous reports based on the in situ TEM method.[27] Third, we could monitor the displacement of individual nanorods (see schematic drawings in Figure 3a, still images from WetSTEM recordings in Figure 3b, and Movie S1 in the Supporting Information), in particular those which were located at the edges of vertical aggregates. These observations correlate well with the bulk-scale observations of thermally driven disassembly for AuNR@MUDOL aggregates and

confirm that we can analyze the process with single-particle precision. In summary, we can safely assume that the WetSTEM experimental conditions are suitable to monitor the dynamic behavior of Au nanorods, which is similar to their macroscale behavior.

Close observation of the vertical assemblies of AuNR@MUDOL allowed us to register, apart from the displacement of individual AuNRs, the detachment, and movement of side-to-side ordered clusters comprising tens of nanoparticles (Figure 3c,d, and Movie S2). Importantly, despite the clusters' dynamic behavior (twisting/turning, finally "swimming" away), AuNRs

therein maintained their initial orientational order. Schematic models and images from three such events are shown in Figure 3c, d (see more examples in the SI, Figure S3a-b and SI Movies S3−S4). This is a striking in situ observation of the colloidal behavior of ordered, relatively large (more than 10 nanoparticles) AuNR clusters. The colloidal stability of such clusters is in agreement with the above UV/vis spectra (Figure 1d) and with the proposed mechanism for the formation of vertical AuNR assemblies, in which side-to-side aggregates are first formed, followed by precipitation from the dispersion and arrangement on a substrate. This behavior also indicates that in our experimental conditions the solvent layer is thick enough to fully cover vertically aligned AuNRs.

We thus conclude that observations of the dynamic behavior of AuNRs in the wet state, at the bulk- and the nanoscale, can be correlated. In both cases, disassembly of AuNR aggregates can be monitored, even though the underlying principles differ. In the SAXRD measurements, disassembly is induced by an increase in temperature (thermal energy), whereas in WetSTEM measurements electrostatic interactions (electron beam-induced charging of the sample) are likely to provide the main driving force for disassembly, since electron beam-induced heating effects are negligible[42,43] (Supplementary Note 2). Given the observed similarities, we investigated the disassembly process of AuNR vertical aggregates from WetSTEM movies. We noted a gradual increase in the distance between AuNRs, under the influence of the electron beam. AuNRs were consistently seen to drift apart from each other prior to rapid disassembly of the clusters into individual AuNRs. Although a detailed analysis of this process within a moving cluster (previously discussed) proved challenging, we could monitor the evolution of larger assemblies.

Therefore, we focused on disassembly events occurring in 2D vertical assemblies, for which AuNRs keep their orientation with respect to the electron beam axis. To minimize differences between observations of separate events we identified assemblies comprising well-ordered clusters made of seven hexagonally arranged nanorods. A schematic model for the process and selected time-lapse frames from sample recordings are shown in Figure 4. These in situ WetSTEM observations allowed us to draw two main conclusions. First, the process of increasing interparticle spacing can be commonly observed in the prepared samples. Second, after reaching a critical interparticle distance, AuNRs start to tremble rapidly and end up losing orientational correlation within their original cluster (Figure 4, multiple such events can be found in Movie S5). We can, therefore, image the evolution of orientational order in clusters of anisotropic nanoparticles, using an in situ EM method. To get a more detailed picture, we quantified our observations by monitoring 2D, hexagonally close-packed structures and calculated the mean separation distance (surface-to-surface) between a central AuNR and six surrounding neighbors forming a 2D hexagonal close-packed structure in the initial state (Figure 4b,d,f and Movies S6−S8). The starting distance, 3−5 nm (Figure 4c,e,g), correlates well with the interparticle distances calculated from SAXRD measurements after subtracting the AuNRs diameter. Under the electron beam, we witnessed an increase of interparticle distance within seconds, accompanied by trembling of AuNRs, while their average positional order was maintained. The loss of orientational correlation between AuNRs was observed at interparticle distances of 7−12 nm, which are slightly larger than twice the length of an extended MUDOL ligand.

Although several factors, such as the presence of neighboring AuNRs, electron beam intensity (at different imaging magnifications), and thickness of the solvent layer, may influence the distance at which positional order is lost, the values estimated on the basis of different recordings are in good agreement.

To understand better the self-assembly and disassembly of the experimental AuNR@MUDOL, we performed hybrid multiscale (MS) modeling of large AuNRs (52 × 16 nm) and separate molecular dynamics (MD) simulations of the disassembly dynamics in small model AuNRs@MUDOL (13 × 4 nm).[44,45]

MS modeling in Figure S4a shows that the large AuNRs have a significant bulk vdW attraction, giving a potential well of ~22 kcal/mol at their surface distances of 3−4 nm. In contrast, small AuNRs have a rather small vdW barrier of a few kcal/mol, which means that their short-range attraction mostly originates from ligand−ligand coupling. These results suggest that AuNRs should self-assemble in water at room temperature due to bulk vdW coupling, and it is unlikely that they would separate without additional repulsion, discussed below. In this context, in Figure S4a, we show the coupling potential energies of large AuNRs with 10 to 130 electron charges per NR, and in Figure S4b we show that the repulsive Coulombic coupling between large charged NRs can decrease the above vdW barrier.

To examine how the potential energy wells shown in Figure S4b change when ligand−ligand coupling is included, we performed molecular modeling of large AuNRs coated with MUDOL ligands. The ligand−ligand coupling free energy between two AuNRs at different surface distances (2.4−5.4 nm), submerged in both water and glycerol, were calculated using solvation free energy calculation with MM/GBSA. For a given NRs distance, the ligand−ligand coupling energies depend on the ligand density and the NRs spatial overlap. For simplicity, the coupling energies are calculated from 5 nm slices of two 52 × 16 nm AuNRs solvated in water ($T = 300$ K) and glycerol ($T = 300$ and 423 K), as shown in Figure 5a (inset on the right).

Figure 5a shows the total interaction free energies ($E_{vdW} + E_C + E_{ligand−ligand}$) of AuNRs (with 130 e charge) submerged in water at 27 °C (300 K). In this case, a potential well of ~220 kcal/mol is obtained in the calculated free energies, which needs to be overcome for the disassembly process to occur. In Figure 5b, we also show calculated total potential free energies for AuNRs submerged in glycerol. Note that the potential free energy well of the system at 150 °C is reduced by 25%, as compared to the system at 27 °C. This clearly indicates a temperature-induced entropic repulsion of the ligands, which can promote disassembly.

To examine more closely the disassembly dynamics of AuNRs, we performed MD simulations of a hexagonal cluster made of seven small model AuNR@MUDOL, while neglecting their bulk vdW coupling (Supplementary Note 3 and Figure S5). The simulations were performed at different temperatures and in different solvents.

The experimental AuNR@MUDOL solvate better in glycerol, where they disassemble above 135 °C. The disassembly of AuNRs might be promoted by entropic effects and NRs charging, leading to a relatively strong repulsion in glycerol. On the other hand, small neutral AuNRs, with partly hydrophobic ligands self-assemble at 25 °C on the water surface, with their tips partly exposed and a surface-to-surface

distance of 3 nm, stabilized by ligand—ligand coupling. This AuNR arrangement was used as the starting point for our stimuli-driven disassembly simulations in which we heated the system or charged the small AuNRs to understand their disassembly dynamics and compare it with the experimental results (Supplementary Notes 4—6).

We simulated small neutral AuNRs@MUDOL submerged in glycerol at 25 and 150 °C (Supplementary Note 4). Whereas in the former case we did not observe disassembly of AuNRs (Figure S6), in the latter (after 28 ns) we did observe their gradual disassembly (Figure 5d and Movie S9). Figure 5e shows that the distance between AuNRs increases from ~3.0 to 4.3 nm. From the experimental point of view, the increased separation distance (5 nm) at higher temperatures (due to entropic ligand repulsion) could be sufficiently advantageous (energetically) for them to overcome the combined vdW and Coulombic barrier (Figure S4b). Larger thermal fluctuations also participate in this process, which can be seen from the evolution of interparticle distances between the top and bottom parts of the nanorods (inset, Figure 5e).

Finally, we addressed the effect of AuNR charging on the the disassembly dynamics. We simulated the process for in situ WetSTEM experiments, where we would not expect heating of the solution, so we could investigate the disassembly of AuNRs induced by e-beam-induced charging (Supplementary Note 5). When considering a charge of 20 e per small AuNR@MUDOL partly or fully submerged in water, no disassembly was observed (Figure S7a-d). However, when charged with 50 e per AuNR@MUDOL, for the fully submerged case, gradual disassembly occurred (Figure 5g and Movie S10). Their average surface-to-surface distance increased from the initial ~3.0 up to 6.1 nm (Figure 5h), while trembling similarly to our in situ experimental observations (inset, Figure 5h). The AuNRs orientation became more disorganized when their separations became roughly twice the ligand length. A similar outcome was observed for AuNRs with the same 50 e charge, which were partially submerged in water (Figure S7e,f). In this case, a radial, more symmetrical path toward AuNRs disassembly was evidenced, which allows AuNRs to keep a hexagonal order during disassembly. In contrast, a more chaotic behavior was evidenced for fully submerged AuNRs, in which the hexagonal order is lost. To maximize the generality of our theoretical framework, we performed additional simulations of AuNR@MUDOL partly or fully submerged in water at 100 °C and observed that these systems did disassemble (Supplementary Note 6, Figure S8a-d, and Table S1). We should keep in mind that despite the dynamics of experimental (large) and MD-simulated (small) NRs are qualitatively similar at the same temperatures and in the same solvents, the disassembly time scales and necessary NRs charging might be much larger in the experimental (large) NRs. That can be clearly expected from the deep potential wells shown in Figure 5 a,b.

It is intriguing to think that, in the context of the experimentally confirmed reversibility of the disassembly process (Figure 2), reversing time in our recordings would enable us to get insight into the assembly process—assembly of single particles as well as clusters of ordered AuNRs (Supporting Information, Movies S11—S12), which is similar to the pre- and postattachment alignment pathways[27] previously reported in the literature for side-to-side assemblies of AuNRs.

CONCLUSIONS

In summary, we carried out a comprehensive study of the (stimuli-responsive) self-assembly of gold nanorods functionalized with MUDOL ligands, into vertical arrays. In situ WetSTEM imaging provided us with a unique, direct insight into this process, showing strong evidence (formation of vertical arrays, and movements of AuNRs) that in situ observations at the single particle level are in agreement with bulk measurements. Notably, we obtained direct proof of the colloidal stability of side-to-side, 2D assemblies of AuNRs, even when in motion. Our approach also allowed us to monitor the disassembly process, which first proceeds with AuNRs keeping orientational order, subsequently losing order after separating to distances larger than double the length of MUDOL ligands. Multiscale modeling enabled us to in silico recreate the thermal- and charge-driven disassembly of AuNRs and to analyze these processes in the context of vdW, Coulombic, and thermal interactions between AuNRs. In conclusion, this work highlights the versatility of the WetSTEM imaging technique for in situ EM studies of NP dynamics and provides insight into the stability orientationally ordered NR assemblies.

EXPERIMENTAL SECTION

Materials. All chemicals were used as received, with no further purification. Gold(III) chloride hydrate (HAuCl$_4$·H$_2$O, 99.995% trace metals basis), hexadecyltrimethylammonium bromide (CTAB, ≥98%), sodium borohydride (NaBH$_4$, powder ≥98%), silver nitrate (AgNO$_3$, ACS reagent, ≥99.0%), 1-mercaptoundec-11-yl)hexa-(ethylene glycol (MUDOL, 90%), and glycerol (ACS reagent, ≥99.5%), were all purchased from Sigma-Aldrich. Milli-Q water (resistivity 18.2 MΩ cm at 25 °C) was used in all experiments. All glassware was washed in aqua regia.

Synthesis of Gold Nanorods. AuNR@CTAB. Gold nanorods were prepared following a previously reported seed-mediated method.[29] In the first step, seeds were prepared as follows: 25 μL of a 0.05 M HAuCl$_4$ solution was added to 4.7 mL of 0.1 M CTAB solution and, after 5 min, 300 μL of a 0.01 M NaBH$_4$ (freshly prepared) solution was injected under vigorous stirring. Then, 120 μL of seed solution was injected to the growth solution containing CTAB 100 mM, HAuCl$_4$ 0.5 mM, AgNO$_3$ 0.04 mM and ascorbic acid 0.75 mM (total volume: 10 mL). The reaction was allowed to proceed undisturbed for 2 h at 30 °C. The obtained AuNRs were on average 51 nm inside length and 15 nm in thickness.

Ligand Exchange on AuNRs. AuNR@MUDOL. A total of 1 mL of MUDOL solution (0.5 mM) was added to 10 mL of Au NRs dispersion (1 mg/mL) in 5 mM CTAB. The reaction mixture was sonicated for 30 min and left under mild stirring overnight. Then, the solution was centrifuged at 3000 rpm for 10 min and the precipitate was redispersed in 2 mL of 5 mM CTAB solution. To transfer AuNR@MUDOL to glycerol, the aqueous dispersion was centrifuged at 3000 rpm for 10 min, and the precipitate redispersed in glycerol under sonication.

Assemblies of Nanorods. For structural analysis, AuNR@MUDOL precipitate was placed in a glass capillary for small angle X — ray diffraction (SAXRD) analysis. Measurements were performed with a Bruker Nanostar system (Cu Kα radiation, parallel beam formed by cross-coupled Goebel mirrors, and a 3-pinhole collimation system, VANTEC 2000 area z detector). Fitting of the obtained diffractogram and simulation of the patterns was performed with Topas 3 software (Bruker). Transmission electron microscopy analysis of AuNRs was performed using TEM model JEM—1400 (JEOL, Japan), available in Nencki Institute of Experimental Biology, Laboratory of electron microscopy. Samples were prepared by drop-casting small aliquots of the as obtained dispersions of AuNRs onto TEM grid, then left to dry under ambient conditions. Spectroscopy in

the UV−vis range studies was performed using GENESYS 50 UV−vis spectrophotometer, available at University of Warsaw.

Modeling Plasmonic Properties of AuNR Assemblies. The Finite-Difference Time-Domain (FDTD) method30 (Lumerical Solutions, Inc.) was used to model the optical properties of single Au NRs and small clusters thereof. All simulations were performed in water (refractive index 1.33). The nanorod dimensions were selected to fit the experimental sample. Dielectric data for gold were obtained by fitting experimental data from Johnson and Christy[47] (0.220 RMS error). All simulations were terminated after reaching a shutoff level of 10^{-6}.

In Situ Electron Microscopy (WetSTEM) Observations. The wet scanning transmission electron microscopy (WetSTEM) system is tailored for high-resolution imaging under conditions of mild pressure and provides the opportunity for in situ dynamic imaging of liquid samples. We used a QUANTA SEM 250 FEG/FEI, equipped with a field emission gun (FEG) system, containing detectors tailored for scanning and transmission imaging in bright- and dark-field. The grid holder is designed for standard 3 mm TEM grids. Furthermore, it provides the possibility to fully control the conditions in the specimen chamber, in terms of temperature and pressure. Our observations were usually carried out at 2 °C, with pressure between 700−1000 Pa, at a landing voltage of 30 kV and low electron flux ranging from 2 to 17e (Å^2 s)$^{-1}$ (Supplementary Note 2), which makes the effect of water radiolysis negligible.[48,49] Since the study was performed on TEM grids, we minimized the impact of electrons backscattered from the support, which could be expected in a regular SEM setup. In a typical experiment, to 100 μL of dispersion of AuNR@MUDOL was added 15 μL of glycerol. Then, an aliquot of the mixture was drop-casted onto a TEM grid previously fixed on the cold (0 °C) WetSEM holder, to make sure that water would not evaporate before closing the equipment and lowering the pressure. After equilibration of the grid for 1 min, the specimen chamber was sealed and the pressure inside was quickly lowered to 1200 Pa and then slowly (10 Pa step) lowered to 700 Pa, to acquire optimal conditions for imaging (lowest obtainable pressure with water remaining in the liquid state on top of the TEM grid). After stabilizing the conditions inside the chamber, the electron beam was turned on for imaging. Videos were recorded at a rate of 50 ns per pixel, with a GSED detector.

Simulation Methods. Self-assembly and disassembly processes of AuNRs were described by hybrid multiscale (MS) modeling for realistic AuNRs, as well as molecular dynamics (MD) simulations for smaller AuNR@MUDOL. Different competing interactions act between solvated AuNRs, such as bulk van der Waals (vdW) coupling, mean electrostatic coupling, ligand−ligand coupling, etc. The effects associated with long-range interactions between AuNRs are captured by the MS method, while their short-range interactions are better described by the MD method.

Multiscale Modeling. Using multiscale methods, we calculated bulk vdW coupling energies E_{vdW} (bulk material of AuNRs), mean electrostatic interaction energies E_c (overall AuNR charging), and atomistic ligand−ligand coupling energies $E_{ligand−ligand}$ between pairs of realistic AuNRs (52 × 16 nm) as a function of their separation in different solvents.

The bulk vdW coupling energy, E_{vdW}, between two AuNRs (52 × 16 nm) was calculated by the Hamaker summation (1) over their volume elements,

$$E_{vdW} = -\frac{A}{\pi^2} \int\int \frac{1}{|r_1 - r_2|^6} \, dr_1 \, dr_2 \tag{1}$$

Here A is the Hamaker constant for Au−Au interaction in water (A = 1.80 eV), and r_1 and r_2 are the position vectors of volume elements on both NRs.

The electrostatic interaction energy, E_c, was calculated by summing over pairs of charged elements, each taken from one of the considered AuNRs, homogeneously distributed on the AuNR surface (modeled as a cylinder) with a thickness 0.5 nm (2),

$$E_c = \int\int \frac{\rho(r_1)\rho(r_2)}{4\pi\varepsilon_0\varepsilon|r_1 - r_2|} \, dr_1 \, dr_2 \tag{2}$$

Here ε = 80 is the dielectric constant of water, $\rho(r_{1,2})$ is a charge density at the position $r_{1,2}$, and $|r_1\text{-}r_2|$ is the distance between both charged elements.

Atomistic Molecular Dynamics Simulations. We have separately simulated the disassembly dynamics in small AuNRs (13 × 4 nm) covered with 300 neutral MUDOL molecules and solvated in water (bulk or surface) and glycerol (400 × 400 × 200 Å^3 or 400 × 400 × 340 Å^3 boxes). AuNR@MUDOL were simulated with Nanoscale Molecular Dynamics (NAMD)[46] in NVT (partially exposed AuNRs, 3 simulations) or NPT (fully submerged AuNRs, 5 simulations) ensembles at T = 300, 373, and 423 K, using the Langevin dynamics with a damping constant of C_{Lang} = 0.1 ps^{-1} and a time step of 2 fs. The CHARMM general force field[50,51] was implemented for the bond, angle, and dihedral parameters of the ligands and solvent molecules. The electrostatic coupling between ions and partially charged atoms (nonbonding interactions) has a cutoff of 1 nm, but the long-range part of this coupling was calculated by the PME method[52] (under periodic boundary conditions). Nonbonding vdW attraction and steric repulsion between molecules were described by Lennard-Jones (LJ) potentials (3),

$$U_{LJ}(r) = \varepsilon\left[\left(\frac{r_{min}}{r}\right)^{12} - 2\left(\frac{r_{min}}{r}\right)^6\right] \tag{3}$$

where ε is the minimum (negative) energy of this coupling and r_{min} is a distance at which $U_{LJ}(r_{min})$ has a local minimum, as provided by the CHARMM force field. The LJ potential implemented in NAMD has a typical cutoff distance of 1 nm (within the solvent).

We also used the atomistic molecular dynamics simulations to track the free energies derived from coupling of segments in large NRs, including ligand−ligand interactions. Toward this end, we constructed a 5 nm-thick slice from two 52 × 16 nm (right inset, Figure 5a) AuNRs coated with MUDOL ligands and submerged in either water (300 K) or glycerol (300 and 423 K). The solvent box in the simulation had dimensions of 320 × 320 × 50 Å^3. The system was first constructed with a surface distance of 5.4 nm. Then, we applied force on one slice, fixed the other slice, and let them approach each other in short simulations. At the desired surface distances, we saved the systems, froze the slices (bulk material) except ligands, and performed MD simulations (described above) on each system for another 10 ns. We then calculated ligand−ligand coupling free energies between the slices (height = 5 nm, diameter = 16 nm) at different surface distances (2.4−5.4 nm) between NRs using solvation free energy calculations with the MMGB-SA method.[53,54] The free energies were averaged over the last 5 ns of the trajectory.

Free energies were estimated from separate MMGB-SA calculations for three systems (two separate AuNR@MUDOL and the self-assembled AuNR@MUDOL complex) in the configurations extracted from the MD trajectories of the whole complex in the given solvent. Then, coupling free energies of NRs were calculated from

$$\Delta G_{bind} = G_{GBSA}(\text{complex}) - G_{GBSA}(\text{separate NRs1})$$
$$- G_{GBSA}(\text{separate NRs1})$$

Free energies were calculated using NAMD 2.13 package generalized Born implicit solvent model,[55] with a dielectric constant of the solvent of 80 and 46.5. The nonpolar contribution for each system configuration was calculated in NAMD as a linear function of the solvent-accessible surface area (SASA), determined using a probe radius of 1.5 Å with a surface tension of γ = 0.00542 kcal/mol Å^{-2}.

■ ASSOCIATED CONTENT

ⓢ Supporting Information

The Supporting Information is available free of charge at https://pubs.acs.org/doi/10.1021/jacs.0c06446.

Supplementary figures and supplementary notes on MD simulations 1−6 (PDF)

Recording from WetSTEM measurements (Movie S1) (MP4)

Recording from WetSTEM measurements (Movie S2) (MP4)

Recording from WetSTEM measurements (Movie S3) (MP4)

Recording from WetSTEM measurements (Movie S4) (MP4)

Recording from WetSTEM measurements (Movie S5) (MP4)

Recording from WetSTEM measurements (Movie S6) (MP4)

Recording from WetSTEM measurements (Movie S7) (MP4)

Recording from WetSTEM measurements (Movie S8) (MP4)

Video from MD simulations (Movie S9) (MPG)

Video from MD simulations (Movie S10) (MP4)

Recording from WetSTEM measurements (Movie S11) (MP4)

Recording from WetSTEM measurements (Movie S12) (MP4)

■ AUTHOR INFORMATION

Corresponding Authors

Petr Král − *Department of Chemistry and Department of Physics, Biopharmaceutical Sciences, and Chemical Engineering, University of Illinois at Chicago, Chicago, Illinois 60607, United States;* ⓞ orcid.org/0000-0003-2992-9027; Email: pkral@uic.edu

Wiktor Lewandowski − *Laboratory of organic nanomaterials and biomolecules, Faculty of Chemistry, University of Warsaw, Warsaw 02-093, Poland; CIC biomaGUNE, Basque Research and Technology Alliance (BRTA) and CIBER-BBN, Donostia, San Sebastián 20014, Spain;* ⓞ orcid.org/0000-0002-3503-2120; Email: wlewandowski@chem.uw.edu.pl

Luis M. Liz-Marzán − *CIC biomaGUNE, Basque Research and Technology Alliance (BRTA) and CIBER-BBN, Donostia, San Sebastián 20014, Spain; Ikerbasque, Basque Foundation for Science, 48013 Bilbao, Spain;* ⓞ orcid.org/0000-0002-6647-1353; Email: llizmarzan@cicbiomagune.es

Authors

Dorota Grzelak − *Laboratory of organic nanomaterials and biomolecules, Faculty of Chemistry, University of Warsaw, Warsaw 02-093, Poland*

Piotr Szustakiewicz − *Laboratory of organic nanomaterials and biomolecules, Faculty of Chemistry, University of Warsaw, Warsaw 02-093, Poland*

Christopher Tollan − *Electron-Microscopy Laboratory, CIC nanoGUNE, Basque Research and Technology Alliance (BRTA), Donostia, San Sebastián 20018, Spain*

Sanoj Raj − *Department of Chemistry, University of Illinois at Chicago, Chicago, Illinois 60607, United States*

Complete contact information is available at:
https://pubs.acs.org/10.1021/jacs.0c06446

Author Contributions
All authors have given approval to the final version of the manuscript.

Notes
The authors declare no competing financial interest.

■ ACKNOWLEDGMENTS

■ REFERENCES

(1) Bodelón, G.; Montes-García, V.; López-Puente, V.; Hill, E. H.; Hamon, C.; Sanz-Ortiz, M. N.; Rodal-Cedeira, S.; Costas, C.; Celiksoy, S.; Pérez-Juste, I.; Scarabelli, L.; La Porta, A.; Pérez-Juste, J.; Pastoriza-Santos, I.; Liz-Marzán, L. M. Detection and Imaging of Quorum Sensing in Pseudomonas Aeruginosa Biofilm Communities by Surface-Enhanced Resonance Raman Scattering. *Nat. Mater.* **2016**, *15*, 1203−1211.

(2) Liu, J.; Guo, J.; Meng, G.; Fan, D. Superstructural Raman Nanosensors with Integrated Dual Functions for Ultrasensitive Detection and Tunable Release of Molecules. *Chem. Mater.* **2018**, *30*, 5256−5263.

(3) Sevenler, D.; Daaboul, G. G.; Ekiz Kanik, F.; Ünlü, N. L.; Ünlü, M. S. Digital Microarrays: Single-Molecule Readout with Interferometric Detection of Plasmonic Nanorod Labels. *ACS Nano* **2018**, *12*, 5880−5887.

(4) Dickerson, E. B.; Dreaden, E. C.; Huang, X.; El-Sayed, I. H.; Chu, H.; Pushpanketh, S.; McDonald, J. F.; El-Sayed, M. A. Gold Nanorod Assisted Near-Infrared Plasmonic Photothermal Therapy (PPTT) of Squamous Cell Carcinoma in Mice. *Cancer Lett.* **2008**, *269*, 57−66.

(5) Li, Z.; Huang, P.; Zhang, X.; Lin, J.; Yang, S.; Liu, B.; Gao, F.; Xi, P.; Ren, Q.; Cui, D. RGD-Conjugated Dendrimer-Modified Gold Nanorods for in Vivo Tumor Targeting and Photothermal Therapy. *Mol. Pharmaceutics* **2010**, *7*, 94−104.

(6) Khalavka, Y.; Becker, J.; Sönnichsen, C. Synthesis of Rod-Shaped Gold Nanorattles with Improved Plasmon Sensitivity and Catalytic Activity. *J. Am. Chem. Soc.* **2009**, *131*, 1871−1875.

(7) Bai, X.; Gao, Y.; Liu, H. G.; Zheng, L. Synthesis of Amphiphilic Ionic Liquids Terminated Gold Nanorods and Their Superior Catalytic Activity for the Reduction of Nitro Compounds. *J. Phys. Chem. C* **2009**, *113*, 17730−17736.

(8) Wu, B.; Liu, D.; Mubeen, S.; Chuong, T. T.; Moskovits, M.; Stucky, G. D. Anisotropic Growth of TiO$_2$ onto Gold Nanorods for Plasmon-Enhanced Hydrogen Production from Water Reduction. *J. Am. Chem. Soc.* **2016**, *138*, 1114−1117.

(9) Gu, M.; Zhang, Q.; Lamon, S. Nanomaterials for Optical Data Storage. *Nat. Rev. Mater.* **2016**, *1*, 16070.

(10) Li, P.; Li, Y.; Zhou, Z. K.; Tang, S.; Yu, X. F.; Xiao, S.; Wu, Z.; Xiao, Q.; Zhao, Y.; Wang, H.; Chu, P. K. Evaporative Self-Assembly of Gold Nanorods into Macroscopic 3D Plasmonic Superlattice Arrays. *Adv. Mater.* **2016**, *28*, 2511−2517.

(11) Hou, S.; Wen, T.; Zhang, H.; Liu, W.; Hu, X.; Wang, R.; Hu, Z.; Wu, X. Fabrication of Chiral Plasmonic Oligomers Using Cysteine-Modified Gold Nanorods as Monomers. *Nano Res.* **2014**, *7*, 1699−1705.

(12) Hamon, C.; Novikov, S.; Scarabelli, L.; Basabe-Desmonts, L.; Liz-Marzán, L. M. Hierarchical Self-Assembly of Gold Nanoparticles

into Patterned Plasmonic Nanostructures. *ACS Nano* **2014**, *8*, 10694−10703.

(13) Evans, J. E.; Jungjohann, K. L.; Browning, N. D.; Arslan, I. Controlled Growth of Nanoparticles from Solution with in Situ Liquid Transmission Electron Microscopy. *Nano Lett.* **2011**, *11*, 2809−2813.

(14) Ahmad, N.; Wang, G.; Nelayah, J.; Ricolleau, C.; Alloyeau, D. Exploring the Formation of Symmetric Gold Nanostars by Liquid-Cell Transmission Electron Microscopy. *Nano Lett.* **2017**, *17*, 4194−4201.

(15) Zhang, D.; Jin, C.; Tian, H.; Xiong, Y.; Zhang, H.; Qiao, P.; Fan, J.; Zhang, Z.; Li, Z. Y.; Li, J. An: In Situ TEM Study of the Surface Oxidation of Palladium Nanocrystals Assisted by Electron Irradiation. *Nanoscale* **2017**, *9*, 6327−6333.

(16) Vadai, M.; Angell, D. K.; Hayee, F.; Sytwu, K.; Dionne, J. A. In-Situ Observation of Plasmon-Controlled Photocatalytic Dehydrogenation of Individual Palladium Nanoparticles. *Nat. Commun.* **2018**, *9*, 4658.

(17) Tan, S. F.; Raj, S.; Bisht, G.; Annadata, H. V.; Nijhuis, C. A.; Král, P.; Mirsaidov, U. Nanoparticle Interactions Guided by Shape-Dependent Hydrophobic Forces. *Adv. Mater.* **2018**, *30*, 1707077.

(18) Woehl, T. J.; Prozorov, T. The Mechanisms for Nanoparticle Surface Diffusion and Chain Self-Assembly Determined from Real-Time Nanoscale Kinetics in Liquid. *J. Phys. Chem. C* **2015**, *119*, 21261−21269.

(19) Liu, Y.; Lin, X. M.; Sun, Y.; Rajh, T. In Situ Visualization of Self-Assembly of Charged Gold Nanoparticles. *J. Am. Chem. Soc.* **2013**, *135*, 3764−3767.

(20) Thorkelsson, K.; Bai, P.; Xu, T. Self-Assembly and Applications of Anisotropic Nanomaterials: A Review. *Nano Today* **2015**, *10*, 48−66.

(21) Kim, J.; Song, X.; Ji, F.; Luo, B.; Ice, N. F.; Liu, Q.; Zhang, Q.; Chen, Q. Polymorphic Assembly from Beveled Gold Triangular Nanoprisms. *Nano Lett.* **2017**, *17*, 3270.

(22) Wei, W.; Bai, F.; Fan, H. Oriented Gold Nanorod Arrays: Self-Assembly and Optoelectronic Applications. *Angew. Chem., Int. Ed.* **2019**, *58*, 11956−11966.

(23) Sutter, E.; Sutter, P.; Tkachenko, A. V.; Krahne, R.; de Graaf, J.; Arciniegas, M.; Manna, L. In Situ Microscopy of the Self-Assembly of Branched Nanocrystals in Solution. *Nat. Commun.* **2016**, *7*, 11213.

(24) Kim, J.; Ou, Z.; Jones, M. R.; Song, X.; Chen, Q. Imaging the Polymerization of Multivalent Nanoparticles in Solution. *Nat. Commun.* **2017**, *8*, 761.

(25) Ou, Z.; Wang, Z.; Luo, B.; Luijten, E.; Chen, Q. Kinetic Pathways of Crystallization at the Nanoscale. *Nat. Mater.* **2020**, *19*, 450−455.

(26) Chen, Q.; Cho, H.; Manthiram, K.; Yoshida, M.; Ye, X.; Alivisatos, A. P. Interaction Potentials of Anisotropic Nanocrystals from the Trajectory Sampling of Particle Motion Using in Situ Liquid Phase Transmission Electron Microscopy. *ACS Cent. Sci.* **2015**, *1*, 33−39.

(27) Tan, S. F.; Anand, U.; Mirsaidov, U. Interactions and Attachment Pathways between Functionalized Gold Nanorods. *ACS Nano* **2017**, *11*, 1633−1640.

(28) Novotný, F.; Wandrol, P.; Proška, J.; Šlouf, M. In Situ WetSTEM Observation of Gold Nanorod Self-Assembly Dynamics in a Drying Colloidal Droplet. *Microsc. Microanal.* **2014**, *20*, 385−393.

(29) Liu, M.; Guyot-Sionnest, P. Mechanism of Silver(I)-Assisted Growth of Gold Nanorods and Bipyramids. *J. Phys. Chem. B* **2005**, *109*, 22192−22200.

(30) Gómez-Graña, S.; Hubert, F.; Testard, F.; Guerrero-Martínez, A.; Grillo, I.; Liz-Marzán, L. M.; Spalla, O. Surfactant (Bi)Layers on Gold Nanorods. *Langmuir* **2012**, *28*, 1453−1459.

(31) Alvarez-Puebla, R. A.; Agarwal, A.; Manna, P.; Khanal, B. P.; Aldeanueva-Potel, P.; Carbó-Argibay, E.; Pazos-Pérez, N.; Vigderman, L.; Zubarev, E. R.; Kotov, N. A.; Liz-Marzán, L. M. Gold Nanorods 3D-Supercrystals as Surface Enhanced Raman Scattering Spectroscopy Substrates for the Rapid Detection of Scrambled Prions. *Proc. Natl. Acad. Sci. U. S. A.* **2011**, *108*, 8157−8161.

(32) Hamon, C.; Postic, M.; Mazari, E.; Bizien, T.; Dupuis, C.; Even-Hernandez, P.; Jimenez, A.; Courbin, L.; Gosse, C.; Artzner, F.; Marchi-Artzner, V. Three-Dimensional Self-Assembling of Gold Nanorods with Controlled Macroscopic Shape and Local Smectic B Order. *ACS Nano* **2012**, *6*, 4137−4146.

(33) Xie, Y.; Guo, S.; Ji, Y.; Guo, C.; Liu, X.; Chen, Z.; Wu, X.; Liu, Q. Self-Assembly of Gold Nanorods into Symmetric Superlattices Directed by OH-Terminated Hexa(Ethylene Glycol) Alkanethiol. *Langmuir* **2011**, *27*, 11394−11400.

(34) Jain, P. K.; Eustis, S.; El-Sayed, M. A. Plasmon Coupling in Nanorod Assemblies: Optical Absorption, Discrete Dipole Approximation Simulation, and Exciton-Coupling Model. *J. Phys. Chem. B* **2006**, *110*, 18243−18253.

(35) Tira, C.; Tira, D.; Simon, T.; Astilean, S. Finite-Difference Time-Domain (FDTD) Design of Gold Nanoparticle Chains with Specific Surface Plasmon Resonance. *J. Mol. Struct.* **2014**, *1072*, 137−143.

(36) Han, B.; Shi, L.; Gao, X.; Guo, J.; Hou, K.; Zheng, Y.; Tang, Z. Ultra-Stable Silica-Coated Chiral Au-Nanorod Assemblies: Core-Shell Nanostructures with Enhanced Chiroptical Properties. *Nano Res.* **2016**, *9*, 451−457.

(37) Chinwangso, P.; Lee, H. J.; Jamison, A. C.; Marquez, M. D.; Park, C. S.; Lee, T. R. Structure, Wettability, and Thermal Stability of Organic Thin-Films on Gold Generated from the Molecular Self-Assembly of Unsymmetrical Oligo(Ethylene Glycol) Spiroalkanedithiols. *Langmuir* **2017**, *33*, 1751−1762.

(38) Cao, H.; Guo, F.; Chen, Z.; Kong, X. Z. Preparation of Thermoresponsive Polymer Nanogels of Oligo(Ethylene Glycol) Diacrylate-Methacrylic Acid and Their Property Characterization. *Nanoscale Res. Lett.* **2018**, *13*, 209.

(39) Can, A.; Zhang, Q.; Rudolph, T.; Schacher, F. H.; Gohy, J. F.; Schubert, U. S.; Hoogenboom, R. Schizophrenic Thermoresponsive Block Copolymer Micelles Based on LCST and UCST Behavior in Ethanol-Water Mixtures. *Eur. Polym. J.* **2015**, *69*, 460−471.

(40) Zorn, S.; Skoda, M. W. A.; Gerlach, A.; Jacobs, R. M. J.; Schreiber, F. On the Stability of Oligo(Ethylene Glycol) (C11EG 6OMe) SAMs on Gold: Behavior at Elevated Temperature in Contact with Water. *Langmuir* **2011**, *27*, 2237−2243.

(41) Kunstmann-Olsen, C.; Belić, D.; Bradley, D. F.; Grzelczak, M. P.; Brust, M. Humidity-Dependent Reversible Transitions in Gold Nanoparticle Superlattices. *Chem. Mater.* **2016**, *28*, 2970−2980.

(42) Kohl, H.; Rose, H.; Schnabl, H. Dose-Rate Effect at Low Temperatures in FBEM and STEM Due to Object-Heating. *Optik (Stuttg).* **1981**, *58*, 11−24.

(43) White, E. R.; Mecklenburg, M.; Shevitski, B.; Singer, S. B.; Regan, B. C. Charged Nanoparticle Dynamics in Water Induced by Scanning Transmission Electron Microscopy. *Langmuir* **2012**, *28*, 3695−3698.

(44) Udayabhaskararao, T.; Altantzis, T.; Houben, L.; Coronado-Puchau, M.; Langer, J.; Popovitz-Biro, R.; Liz-Marzán, L. M.; Vukovic, L.; Král, P.; Bals, S.; Klajn, R. Tunable Porous Nanoallotropes Prepared by Post-Assembly Etching of Binary Nanoparticle Superlattices. *Science* **2017**, *358*, 514−518.

(45) Nitka, T. A.; Král, P.; Vuković, L. Configurations of Nanocubes Floating and Clustering on Liquid Surfaces. *J. Phys. Chem. Lett.* **2019**, *10*, 3592−3597.

(46) Phillips, J. C.; Braun, R.; Wang, W.; Gumbart, J.; Tajkhorshid, E.; Villa, E.; Chipot, C.; Skeel, R. D.; Kalé, L.; Schulten, K. Scalable Molecular Dynamics with NAMD. *J. Comput. Chem.* **2005**, *26*, 1781−1802.

(47) Johnson, P. B.; Christy, R. W. Optical Constatnts for Noble Metals. *Phys. Rev. B* **1972**, *6*, 4370.

(48) Wang, M.; Park, C.; Woehl, T. J. Quantifying the Nucleation and Growth Kinetics of Electron Beam Nanochemistry with Liquid Cell Scanning Transmission Electron Microscopy. *Chem. Mater.* **2018**, *30*, 7727−7736.

(49) Woehl, T. J.; Abellan, P. Defining the Radiation Chemistry during Liquid Cell Electron Microscopy to Enable Visualization of

Nanomaterial Growth and Degradation Dynamics. *J. Microsc.* **2017**, *265*, 135−147.

(50) Yu, W.; He, X.; Vanommeslaeghe, K.; MacKerell, A. D. Extension of the CHARMM General Force Field to Sulfonyl-Containing Compounds and Its Utility in Biomolecular Simulations. *J. Comput. Chem.* **2012**, *33*, 2451−2468.

(51) Allouche, A. Software News and Updates Gabedit — A Graphical User Interface for Computational Chemistry Softwares. *J. Comput. Chem.* **2011**, *32*, 174−182.

(52) Darden, T.; York, D.; Pedersen, L. Particle Mesh Ewald: An N·log(N) Method for Ewald Sums in Large Systems. *J. Chem. Phys.* **1993**, *98*, 10089−10092.

(53) Homeyer, N.; Gohlke, H. Free Energy Calculations by the Molecular Mechanics Poisson-Boltzmann Surface Area Method. *Mol. Inf.* **2012**, *31*, 114−122.

(54) Vergara-Jaque, A.; Comer, J.; Monsalve, L.; González-Nilo, F. D.; Sandoval, C. Computationally efficient methodology for atomic-level characterization of dendrimer-drug complexes: A comparison of amine- and acetyl-terminated PAMAM. *J. Phys. Chem. B* **2013**, *117*, 6801−6813.

(55) Tanner, D. E.; Chan, K. Y.; Phillips, J. C.; Schulten, K. Parallel Generalized Born Implicit Solvent Calculations with NAMD. *J. Chem. Theory Comput.* **2011**, *7*, 3635−3642.